


Magnetic Confinement of an Ultracold Neutral Plasma

G. M. Gorman¹, M. K. Warrens¹, S. J. Bradshaw¹, and T. C. Killian^{1*}

Department of Physics and Astronomy, Rice University, Houston, Texas 77005, USA

 (Received 10 November 2020; revised 5 January 2021; accepted 22 January 2021; published 25 February 2021)

We demonstrate magnetic confinement of an ultracold neutral plasma (UCNP) created at the null of a biconic cusp, or quadrupole magnetic field. Initially, the UCNP expands due to electron thermal pressure. As the plasma encounters stronger fields, expansion slows and the density distribution molds to the field. UCNP electrons are strongly magnetized over most of the plasma, while ion magnetization is only significant at the boundaries. Observations suggest that electrons and ions are predominantly trapped by magnetic mirroring and ambipolar electric fields, respectively. Confinement times approach 0.5 ms, while unmagnetized plasmas dissipate on a timescale of a few tens of microseconds.

DOI: [10.1103/PhysRevLett.126.085002](https://doi.org/10.1103/PhysRevLett.126.085002)

The biconic cusp, or quadrupole magnetic field configuration, formed by anti-Helmholtz current coils [1,2] can confine neutral plasmas near the central null-field region due to the magnetic-mirror effect [3]. This confinement scheme has been of long-standing interest, initially for magnetic-confinement fusion [1,2,4–6], and more recently for ion sources for applications such as material processing and ion thrusters [7–9]. Neutral plasma expanding across biconic cusp field lines experiences changing length scales and dominant physical processes, and the complex geometry has similarity to the solar wind interacting with Earth's magnetosphere [2,10]. Here, we demonstrate the magnetic confinement of an ultracold neutral plasma (UCNP) [11–13] created at the null point of a biconic cusp field [Fig. 1(a)].

UCNPs, created here by photoionizing laser-cooled Sr atoms near the ionization threshold, have ion temperatures $T_i \sim 1$ K and tunable electron temperatures of $T_e = 1$ –1000 K, which offers a novel regime for study of magnetized and magnetically confined neutral plasmas. UCNPs also provide the opportunity to study the combined effects of magnetization and strong coupling on collisional and transport phenomena because ions are strongly coupled in UCNPs, with the ratio of Coulomb energy to kinetic energy, known as the Coulomb coupling parameter [14], as high as $\Gamma_i = 11$ [15–17]. Electrons can also approach the strongly coupled regime, with $\Gamma_e \lesssim 0.4$ [18–22]. There is emerging focus on magnetized and strongly coupled plasmas in general [23,24] and in the ultracold regime [24–26], driven in large part by new experimental capabilities in dusty [27–29] and laser-produced high-energy-density plasmas [30,31].

Previous experimental work with magnetized UCNPs is limited. A pioneering experiment studied cross-field ambipolar diffusion in a uniform field strong enough to magnetize electrons but not ions [32]. The same authors [33] identified a high-frequency electron drift instability in weak, crossed magnetic and electric fields. Non-neutral

plasmas are routinely confined in combined electric and magnetic fields in Penning-Malmberg traps [34], and these techniques have been extended to confine partially overlapping clouds of positive and negative charges at ultracold temperatures in nested traps, such as for antihydrogen production [35,36]. Dynamics of a UCNP loaded into such a trap, forming partially overlapping electron and ion components, was studied in Ref. [37].

To create a UCNP, Sr atoms are first laser cooled and confined with a magneto-optical trap (MOT) using the $5s^2\ ^1S_0 - 5s5p\ ^1P_1$ transition at 461 nm. Atoms populate the metastable $5s5p\ ^3P_2$ state throughout the laser-cooling process due to a weak decay path from the cycling transition, and low-field seeking 3P_2 atoms ($m_j = +2, +1$) are magnetically trapped in the quadrupole magnetic field of the MOT due to their large magnetic moment [38]. 3P_2 atoms are then photoionized near threshold with 322-nm photons from a 10-ns pulsed dye laser. The plasma inherits its initial density distribution, $n(\vec{r}) = n_0 \exp(-\sqrt{x^2 + y^2/4 + z^2/4}/\alpha)$, from the magnetically trapped neutral atoms, with $\alpha = 3k_B T_a / 8\mu_B B' \approx 1$ mm, where $T_a \approx 3$ mK is the temperature of the neutral atoms, $B' = 150$ G/cm is the gradient of the magnetic field along the symmetry (x) axis, and μ_B and k_B are the Bohr magneton and Boltzmann constant, respectively. The atom cloud is small compared to the radius of the coils creating the magnetic field, so a linear approximation of the field profile is sufficient.

Initial peak density ($n_0 \sim 10^9$ cm⁻³) is controlled by varying the laser-cooling time (~ 1 s) to vary the number of trapped atoms. The same quadrupole field used to laser cool and trap the precursor atoms is used to magnetically confine the plasma. Plasma dynamics without magnetic field are studied by extinguishing the field over a 280 μ s period prior to photoionization.

Because of the large electron-ion mass ratio, essentially all of the excess photoionization energy is converted to

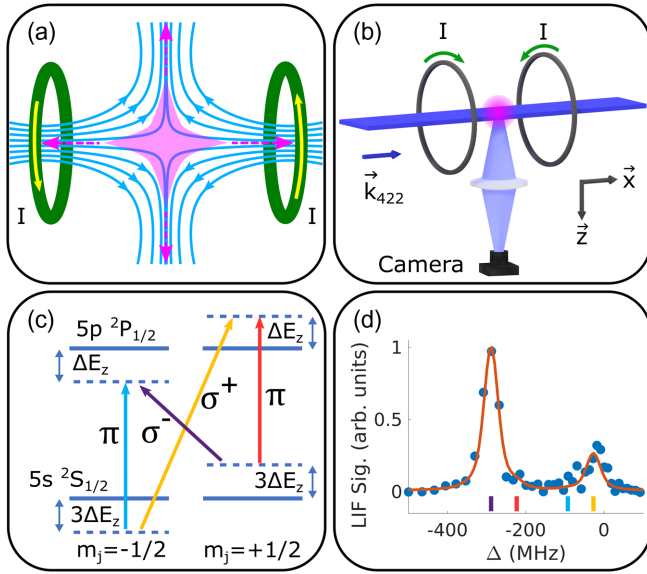


FIG. 1. (a) Anti-Helmholtz coils, magnetic field lines, and confined plasma in a biconic cusp field. Horizontal dashed arrows indicate loss along the symmetry (x) axis and vertical dashed arrows indicate a loss circle in the y - z plane. (b) Experimental schematic for laser-induced fluorescence (LIF) imaging and application of magnetic fields. The plasma is illuminated by a thin sheet of 422-nm light that propagates along the x axis and is linearly polarized along the y axis. The ion fluorescence is imaged onto an intensified CCD camera using a 1 : 1 optical relay along the z axis. (c) Sr levels involved in LIF with (dashed lines) and without (solid lines) Zeeman shifts. (d) LIF spectrum of a magnetized UCNP at $x = 4.6$ mm and $y = 1.6$ mm (origin at plasma center), where $B = 70$ G and the LIF laser drives the σ transitions equally and the π transitions are driven relatively weakly. The asymmetry in the spectrum reflects ion spin polarization.

electron thermal energy. Thus, the initial electron temperature, $T_e = 20$ – 160 K, is set by the photoionization laser detuning above threshold, calibrated using iodine absorption spectroscopy. Ions are created with extremely low kinetic energy, close to that of the precursor neutral atoms, but they possess significant potential energy due to their initially uncorrelated state and undergo a process called disorder-induced heating in the first few 100 ns. This results in ion temperatures $T_i \sim 1$ K [15,39].

The plasma is probed at an adjustable time after photoionization using laser-induced fluorescence (LIF) on the $5s^2S_{1/2} - 5p^2P_{1/2}$ transition of Sr^+ at 422 nm [40]. The LIF laser, with detuning Δ from unperturbed resonance, illuminates a 1-mm-thick central slice of the plasma ($z \approx 0$) [Fig. 1(b)]. Scattered photons are imaged onto an intensified CCD camera to obtain a spatially resolved LIF fluorescence spectrum, $F(x, y, \Delta)$, with $50 \mu\text{m}$ resolution. Each image consists of photons collected over a 0.5 – $2 \mu\text{s}$ time period that is set by CCD and LIF-laser gating. Image times indicated in all figures refer to the midway point of the imaging window.

The LIF spectrum is modeled using a Fermi's golden rule description of the fluorescence line shape [40] including Zeeman shifts, which is convolved with the local ion velocity distribution, assuming local thermal equilibrium. The local hydrodynamic fluid velocity along the LIF-laser propagation direction ($v_{x,\text{hyd}}$) and ion temperature (T_i) manifest as a mean shift and broadening of the single-particle fluorescence line shape, respectively, and the local ion density (n) is derived from the integral of the spectrum [40]. We extract measurements of n , T_i , and $v_{x,\text{hyd}}$ by fitting $F(x, y, \Delta)$ with the LIF spectrum model. For magnetized UCNPs, the lower and upper states of the LIF transition each display Zeeman splittings [Fig. 1(c)], and the strengths of different Zeeman components reflect the initial spin polarization of the ions and decomposition of the LIF-laser polarization in the coordinate frame of the local magnetic field. Figure 1(d) shows an example of such a fit. Asymmetric spectra are observed consistently across the plasma spatially and during the entire plasma evolution, indicating long-lived polarization of the spin of the valence electron of each Sr^+ ion along the local magnetic field. Polarization arises because the precursor magnetically trapped atoms possess a high degree of spin polarization.

In a UCNP, when magnetic forces are absent or negligible, electron thermal pressure drives plasma expansion on a characteristic hydrodynamic timescale of $\tau_{\text{exp}} = \sqrt{m_i \sigma(0)^2 / k_B T_e(0)}$, where m_i is the Sr^+ mass and $\sigma(0)$ and $T_e(0)$ are the initial geometric mean rms plasma radius and electron temperature, respectively [20,41]. This phenomenon has traditionally been studied with UCNPs with spherically symmetric Gaussian density distributions [42]. The expansion velocity field for Gaussian plasmas increases with distance from plasma center and time after photoionization (t), following $\vec{v}_{\text{hyd}} = \gamma(t)\vec{r}$, where $\gamma(t) = t / [\tau_{\text{exp}}^2 (1 + t^2 / \tau_{\text{exp}}^2)]$ [42–44]. This description applies reasonably well for exponentially decaying density distributions as used here [45].

Figure 2 shows the evolution of plasma density and $v_{x,\text{hyd}}$ without and with magnetic fields for a UCNP with $T_e(0) = 20$ K and $\sigma(0) = 1.3$ mm ($\tau_{\text{exp}} = 30 \mu\text{s}$). The data in Fig. 2 are obtained by fitting the Fermi's golden rule model to local spectra that were averaged over 20–60 realizations of the plasma (more images were used for longer expansion times). A 2D Gaussian smoothing filter with rms width 0.2 mm was used to filter out high-frequency noise components. Initially ($t = 1.5 \mu\text{s}$), the plasma density and velocity distributions without [Figs. 2(a) and 2(c)] and with [Figs. 2(b) and 2(d)] the fields are nearly identical and the plasma has not yet developed significant expansion velocity.

At early times ($t < \tau_{\text{exp}}$), outward hydrodynamic pressure dominates and the expansion is relatively unaffected by the magnetic fields. This is reflected by the nearly identical density distributions at $t = 29 \mu\text{s}$. However, while constant $v_{x,\text{hyd}}$ along lines of constant x is observed without

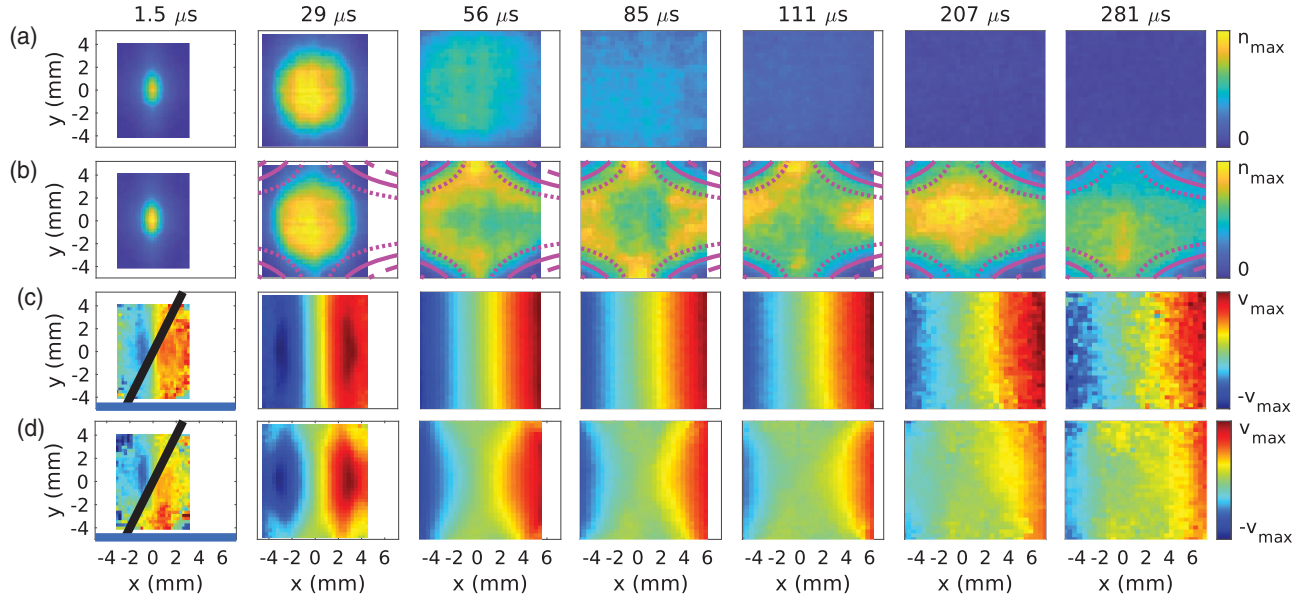


FIG. 2. Plasma expansion without and with magnetic field ($B' = 150\text{G/cm}$) for $T_e(0) = 20\text{ K}$. Rows (a) and (b) show density distributions without and with field, respectively. The lines in row (b) (dotted, solid, and dashed) correspond to sample field lines. Time after plasma creation is indicated above each column. The scale for the density color bar for each time point is $n_{\text{max}} = [13.8, 1.7, 0.59, 0.36, 0.25, 0.18, 0.18] \times 10^8\text{ cm}^{-3}$, in order of increasing time. Rows (c) and (d) show the x component of the hydrodynamic velocity $v_{x,\text{hyd}}$ without and with magnetic fields, respectively. The scale for the velocity color bar for each time point is $v_{\text{max}} = [10, 70, 100, 75, 62, 35, 25]\text{ m/s}$. The black and blue lines in the first time point of rows (c) and (d) correspond to $y = 2x$ and $y = -4.8\text{ mm}$, respectively. Figure 3 plots $v_{x,\text{hyd}}$ along each of these lines.

fields as expected for $\vec{v}_{\text{hyd}} \propto \vec{r}$, velocity retardation is evident for ions traversing field lines in regions far from plasma center where the fields are large. For example, along the $y = 2x$ and $y = -4.8\text{ mm}$ lines [indicated in Figs. 2(c) and 2(d), $t = 1.5\text{ }\mu\text{s}$], magnetic forces have clearly impeded the expansion by $t = 29\text{ }\mu\text{s}$. This is highlighted in the velocity transects shown in Fig. 3. Along the x axis, where plasma expansion velocity is parallel to the field lines, $v_{x,\text{hyd}}$ is still unaffected by fields.

By $t = 85\text{ }\mu\text{s}$ the no-fields plasma appears uniform because the plasma size exceeds the imaged region. Gradients in plasma density that produce outward electron thermal pressure have diminished, leading to a ballistic plasma expansion for no fields that persists throughout the rest of the expansion (green line in Fig. 3 representing $v_{x,\text{hyd}} = x/t$).

The with-fields plasma shows considerable effects of the magnetic fields during this intermediate time. The plasma begins to develop a boundary that follows a field line [Fig. 2(b)]. Expansion near the plasma center is relatively unaffected because of the weak fields, leading to a central plasma depletion and a buildup of plasma density at the boundary. The effects on the plasma velocity, evident at earlier times, become stronger. Most striking is a reversal of $v_{x,\text{hyd}}$ in regions of strong field where the expansion velocity is close to perpendicular to field lines, such as near $x \pm 2\text{ mm}$ for $y = -4.8\text{ mm}$. The velocity reversal is subtle in Fig. 2(d), but is easier to discern in Fig. 3

(bottom). The combined density and velocity information indicates that plasma flow across field lines in these regions has halted, and is now redirected along field lines back toward $x = 0$ and increasing $|y|$ for $|x| \lesssim 2\text{ mm}$.

The initial expansion of the UCNP is driven by gradients in the hydrodynamic electron thermal pressure [12], which creates a force per ion of

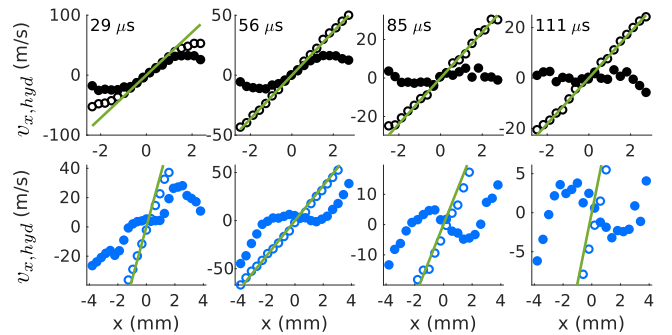


FIG. 3. Evolution of the x component of hydrodynamic velocity for plasma along the lines $y = 2x$ (top) and $y = -4.8\text{ mm}$ (bottom) for data shown in Fig. 2 for plasmas evolving without (open symbols) and with (closed symbols) magnetic fields. The solid green line represents $v_{x,\text{hyd}} = x/t$, the ion velocity expected for $\vec{v}_{\text{hyd}} = \gamma(t)\vec{r}$ or ballistic expansion at late times ($t \gg \tau_{\text{exp}}$). Time since plasma creation is indicated above each column.

$$\vec{F}_{\text{exp}}(\vec{r}, t) = -\frac{\nabla n(\vec{r})}{n(\vec{r})} k_B T_e(t), \quad (1)$$

where $T_e(t)$ is the electron temperature, which decreases during expansion due to adiabatic cooling. The UCNP expansion may equivalently be described as ambipolar diffusion, where the electrons and ions diffuse together at the ion acoustic velocity. Deviations between no-fields and with-fields plasma velocity for ions crossing field lines are observed as early as $t = 29 \mu\text{s}$ (for example, along the velocity transects in Fig. 3). The Lorentz force that the fields exert on charged particles of species s due to the expansion velocity, $\vec{F}_{Ls}(\vec{r}, t) = q_s \vec{v}_{x,\text{hyd}}(\vec{r}, t) \times \vec{B}(\vec{r})$, is negligible compared to \vec{F}_{exp} at this time, and is not responsible for the velocity reduction.

However, at the boundary of the with-fields plasma, where the effects of the magnetic field on the expansion first appear, the magnetization of the plasma is significant, as characterized by the magnetization parameter $\delta = \rho/L$, the ratio of thermal gyroradius $\rho = \sqrt{k_B T_s m_s}/eB$ to the characteristic length scale of the plasma $n(\vec{r})/\nabla n(\vec{r}) \equiv L \sim 1 \text{ mm}$. For $B \approx 50 \text{ G}$ and $T_e = 10 \text{ K}$, $\rho_e = 10 \mu\text{m}$, indicating the electrons are strongly magnetized. For ions with $T_i = 0.25 \text{ K}$, the magnetization is modest, with $\rho_i \approx L$. This suggests that the reduction of cross-field expansion results from pinning of the strongly magnetized electrons to field lines. Assuming classical diffusion [32], the transverse diffusion constant is $D_{\perp} = \rho_e^2 \nu_{ei} \approx 1 \text{ mm}^2/\text{ms}$, for ion density $n_i = 2 \times 10^7 \text{ cm}^{-3}$, where $\nu_{ei} \propto n_i/T_e^{3/2}$ is the electron-ion collision rate. Cross-field diffusion several millimeters from the field null should thus be slow on the timescale of these experiments, as observed.

At late times (Fig. 2, $t > 150 \mu\text{s} \sim 5\tau_{\text{exp}}$), the expansion for the magnetized plasma has essentially halted and the plasma has become magnetically trapped, with a density maximum in the plasma center. Magnetic confinement arises from the magnetic mirror effect, which results from conservation of the adiabatic invariant $\mu \equiv m_s v_{\perp}^2/2B$ for a charged particle moving along a guiding field line, where v_{\perp} is the particle's velocity transverse to the local field. The force per particle is $\vec{F}_{\parallel} = -\hat{\ell} \mu \partial B/\partial \ell$ pointing in the direction of decreasing field strength, where ℓ is the distance along the field line. Particles with large enough μ and small enough total kinetic energy \mathcal{E} , described as having a large pitch angle, are trapped between bounce points where $B = \mathcal{E}/\mu$.

Ion motion for plasma regions imaged in Fig. 2 is not adiabatic, but electron motion is adiabatic everywhere except close to the field null. Thus, as expected for biconic cusp fields [1,2,6,46], the likely description of UCNP trapping is that electrons move along field lines, confined between bounce points. Ambipolar electric fields transverse to magnetic field lines constrain ion cross-field transport. Electrons with large enough \mathcal{E}/μ escape through loss gaps around the field maxima along field lines in the y - z plane and along the x symmetry axis [Fig. 1(a)]. This

loss is fed by nonadiabatic mixing of electron trajectories near the field null and by collisions. In the loss gaps, ambipolar fields slow electrons, leading to plasma loss at ion acoustic velocities $\propto \sqrt{T_e/m_i}$ [46].

To characterize the onset of confinement and rate of plasma loss, Fig. 4 shows the time evolution of the central plasma density $n_c(t)$ relative to its initial value. Time is scaled by the characteristic hydrodynamic timescale. A $1/t^3$ fit to data with $t > 4\tau_{\text{exp}}$ demonstrates the ballistic nature of plasma expansion without fields at late times.

In contrast, the with-fields (closed symbol) central density stabilizes at $n_c(t)/n_c(0) = 10^{-2}$ at $t = 5\tau_{\text{exp}}$ (see Fig. 4). Developing a quantitative explanation for this universal behavior will be the subject of future study, but it is generally consistent with the onset of trapping occurring when the average hydrodynamic expansion force [Eq. (1)], which decreases rapidly with time, matches the typical magnetic mirror force. While the onset time and level of trapping in scaled units shows no discernible dependence on density, the trap lifetime decreases for higher $T_e(0)$, which is consistent with plasma loss through loss gaps at the ion acoustic speed. The solid and dashed lines in Fig. 4 are exponential fits to $T_e = 40 \text{ K}$ and $T_e = 160 \text{ K}$ data, respectively, which reveal magnetic confinement timescales of $500 \mu\text{s}$ (40 K) and $100 \mu\text{s}$ (160 K).

This work demonstrates magnetic confinement of a UCNP in a biconic cusp magnetic field. The plasma density and velocity-field profiles and estimates of relevant forces imply that the plasma confinement results from strongly magnetized electrons following guiding field lines and ions constrained by ambipolar fields. Observed trap lifetimes decrease with increasing electron temperature, which is consistent with a dominant loss mechanism of flux through the loss gaps.

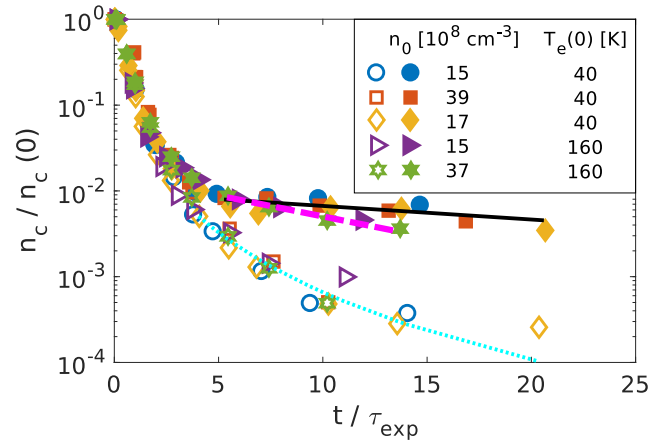


FIG. 4. Relative plasma density in the plasma center versus time scaled by the hydrodynamic expansion timescale (τ_{exp}) without (open symbols) and with (closed symbols) magnetic field. Solid and dashed lines are exponential fits to $T_e(0) = 40 \text{ K}$ and $T_e(0) = 160 \text{ K}$ with-fields data, respectively, for $t > 5\tau_{\text{exp}}$. The dotted line is a $1/t^3$ fit to all no-fields data with $t > 4\tau_{\text{exp}}$. Initial peak density and electron temperature are indicated in the legend.

The magnetic confinement of UCNP opens many new research directions. UCNP have long been used for experimental studies of the effects of strong coupling on collisional transport processes [47], and these new capabilities may enable exploration of overlapping regimes of strong coupling and magnetization [23,24]. With experimental improvements such as increased magnetic field gradient and field of view for LIF imaging, it should be possible to characterize scaling of trapping behavior with magnetic field and study plasma flow in loss gaps, which will support development of a quantitative model of plasma dynamics. The combination of magnetic trapping with recently demonstrated techniques of laser cooling of UCNP ions [17] appears promising for improving laser-cooling efficacy. Because the loss processes for the biconic cusp trap are localized along loss gaps, laser-induced forces should be particularly effective for plugging the loss in this geometry, perhaps leading to significantly enhanced trap lifetimes.

This work was supported by the U.S. Air Force Office of Scientific Research through Grant No. FA9550-17-1-0391 and the National Science Foundation Graduate Research Fellowship Program under Grant No. 1842494.

*Corresponding author.
killian@rice.edu

- [1] J. Berkowitz, K. O. Friedrichs, H. Goertzel, H. Grad, J. Killeen, and E. Rubin, in *Proceedings of the Second International Conference on Peaceful Uses of Atomic Energy, Geneva, Switzerland*, Vol. 1 (United Nations, Geneva, 1958), p. 177.
- [2] I. Spalding, in *Advances in Plasma Physics*, Vol. 4, edited by A. Simon and W. B. Thompson (Interscience, New York, 1971), p. 79.
- [3] R. F. Post, R. E. Ellis, F. C. Ford, and M. N. Rosenbluth, *Phys. Rev. Lett.* **4**, 166 (1960).
- [4] M. G. Haines, *Nucl. Fusion* **17**, 811 (1977).
- [5] A. Kitsunezaki, M. Tanimoto, and T. Sekiguchi, *Phys. Fluids* **17**, 1895 (1974).
- [6] K. N. Leung, N. Hershkowitz, and K. R. MacKenzie, *Phys. Fluids* **19**, 1045 (1976).
- [7] M. Carr, D. Gummertsall, S. Cornish, and J. Khachan, *Phys. Plasmas* **18**, 112501 (2011).
- [8] C. M. Cooper, D. B. Weisberg, I. Khalzov, J. Milhone, K. Flanagan, E. Peterson, C. Wahl, and C. B. Forest, *Phys. Plasmas* **23**, 102505 (2016).
- [9] A. A. Hubble, E. V. Barnat, B. R. Weatherford, and J. E. Foster, *Plasma Sources Sci. Technol.* **23**, 022001 (2014).
- [10] C. T. Russell, *IEEE Trans. Plasma Sci.* **28**, 1818 (2000).
- [11] T. C. Killian, S. Kulin, S. D. Bergeson, L. A. Orozco, C. Orzel, and S. L. Rolston, *Phys. Rev. Lett.* **83**, 4776 (1999).
- [12] T. C. Killian, T. Pattard, T. Pohl, and J. M. Rost, *Phys. Rep.* **449**, 77 (2007).
- [13] M. Lyon and S. L. Rolston, *Rep. Prog. Phys.* **80**, 017001 (2017).
- [14] S. Ichimaru, *Rev. Mod. Phys.* **54**, 1017 (1982).
- [15] C. E. Simien, Y. C. Chen, P. Gupta, S. Laha, Y. N. Martinez, P. G. Mickelson, S. B. Nagel, and T. C. Killian, *Phys. Rev. Lett.* **92**, 143001 (2004).
- [16] M. Lyon, S. D. Bergeson, and M. S. Murillo, *Phys. Rev. E* **87**, 033101 (2013).
- [17] T. K. Langin, G. M. Gorman, and T. C. Killian, *Science* **363**, 61 (2019).
- [18] S. G. Kuzmin and T. M. O'Neil, *Phys. Plasmas* **9**, 3743 (2002).
- [19] S. Mazevet, L. A. Collins, and J. D. Kress, *Phys. Rev. Lett.* **88**, 055001 (2002).
- [20] F. Robicheaux and J. D. Hanson, *Phys. Rev. Lett.* **88**, 055002 (2002).
- [21] P. Gupta, S. Laha, C. E. Simien, H. Gao, J. Castro, T. C. Killian, and T. Pohl, *Phys. Rev. Lett.* **99**, 075005 (2007).
- [22] W. T. Chen, C. Witte, and J. L. Roberts, *Phys. Rev. E* **96**, 013203 (2017).
- [23] T. Ott and M. Bonitz, *Phys. Rev. Lett.* **107**, 135003 (2011).
- [24] S. D. Baalrud and J. Daligault, *Phys. Rev. E* **96**, 043202 (2017).
- [25] I. L. Isaev and A. P. Gavriiliuk, *J. Phys. B* **51**, 025701 (2018).
- [26] S. K. Tiwari and S. D. Baalrud, *Phys. Plasmas* **25**, 013511 (2018).
- [27] E. Thomas, R. L. Merlino, and M. Rosenberg, *Plasma Phys. Controlled Fusion* **54**, 124034 (2012).
- [28] V. Y. Karasev, E. S. Dzhlieva, L. G. D'yachkov, L. A. Novikov, S. I. Pavlov, and S. A. Tarasov, *Controlled Plasma Phys.* **59**, e201800136 (2019).
- [29] Y. Feng, S. Lu, K. Wang, W. Lin, and D. Huang, *Rev. Mod. Phys.* **3**, 10 (2019).
- [30] Y. Shi, H. Qin, and N. Fisch, *Phys. Plasmas* **25**, 055706 (2018).
- [31] J. J. Santos *et al.*, *Phys. Plasmas* **25**, 056705 (2018).
- [32] X. L. Zhang, R. S. Fletcher, S. L. Rolston, P. N. Guzdar, and M. Swisdak, *Phys. Rev. Lett.* **100**, 235002 (2008).
- [33] X. L. Zhang, R. S. Fletcher, and S. L. Rolston, *Phys. Rev. Lett.* **101**, 195002 (2008).
- [34] D. H. E. Dubin and T. M. O'Neil, *Rev. Mod. Phys.* **71**, 87 (1999).
- [35] M. Amoretti *et al.*, *Nature (London)* **419**, 456 (2002).
- [36] G. Gabrielse *et al.*, *Phys. Rev. Lett.* **89**, 213401 (2002).
- [37] J. H. Choi, B. Knuffman, X. H. Zhang, A. P. Povilus, and G. Raithel, *Phys. Rev. Lett.* **100**, 175002 (2008).
- [38] S. B. Nagel, C. E. Simien, S. Laha, P. Gupta, V. S. Ashoka, and T. C. Killian, *Phys. Rev. A* **67**, 011401(R) (2003).
- [39] M. S. Murillo, *Phys. Rev. Lett.* **87**, 115003 (2001).
- [40] J. Castro, H. Gao, and T. C. Killian, *Plasma Phys. Controlled Fusion* **50**, 124011 (2008).
- [41] S. Kulin, T. C. Killian, S. D. Bergeson, and S. L. Rolston, *Phys. Rev. Lett.* **85**, 318 (2000).
- [42] S. Laha, P. Gupta, C. E. Simien, H. Gao, J. Castro, T. Pohl, and T. C. Killian, *Phys. Rev. Lett.* **99**, 155001 (2007).
- [43] A. V. Baitin and K. M. Kuzanyan, *J. Plasma Phys.* **59**, 83 (1998).
- [44] D. S. Dorozhkina and V. E. Semenov, *Phys. Rev. Lett.* **81**, 2691 (1998).
- [45] M. K. Warrens, G. M. Gorman, S. J. Bradshaw, and T. C. Killian, *Phys. Plasmas* **28**, 022110 (2021).
- [46] R. A. Bosch and R. L. Merlino, *Phys. Fluids* **29**, 1998 (1986).
- [47] S. D. Bergeson, S. D. Baalrud, C. Leland Ellison, E. Grant, F. R. Graziani, T. C. Killian, M. S. Murillo, J. L. Roberts, and L. G. Stanton, *Phys. Plasmas* **26**, 100501 (2019).